

Hybrid NeRF-Stereo Vision: Pioneering Depth Estimation and 3D Reconstruction in Endoscopy

Pengcheng Chen*

¹University of Washington
pengcc@uw.edu

Wenhai Li*

³Artificial Intelligence and Robotics for Society (AIRS)
⁴SSE, The Chinese University of Hong Kong (Shenzhen)
wenhaoli1@link.cuhk.edu.cn

Nicole Gunderson¹

¹University of Washington
nmgundo@uw.edu

Jeremy Ruthberg²

² Otolaryngology, University of Washington
jruthb@uw.edu

Randall Bly²

² Otolaryngology, University of Washington
randbly@uw.edu

Waleed M. Abuzeid²

² Otolaryngology, University of Washington
wabuzeid@uw.edu

Zhenglong Sun⁴

⁴SSE, The Chinese University of Hong Kong (Shenzhen)
sunzhenglong@cuhk.edu.cn

Eric J. Seibel¹

¹University of Washington
eseibel@uw.edu

Abstract

The 3D reconstruction of the surgical field in minimally invasive endoscopic surgery has posed a formidable challenge when using conventional monocular endoscopes. Existing 3D reconstruction methodologies are frequently encumbered by suboptimal accuracy and limited generalization capabilities. In this study, we introduce an innovative pipeline using Neural Radiance Fields (NeRF) for 3D reconstruction. Our approach utilizes a preliminary NeRF reconstruction that yields a coarse model, then creates a binocular scene within the reconstructed environment, which derives an initial depth map via stereo vision. This initial depth map serves as depth supervision for subsequent NeRF iterations, progressively refining the 3D reconstruction with enhanced accuracy. The binocular depth is iteratively recalculated, with the refinement process continuing until the depth map converges, and exhibits negligible variations. Through this recursive process, high-fidelity depth maps are generated from monocular endoscopic video of a realistic cranial phantom. By repeated measures of the final 3D reconstruction compared to X-ray computed tomography, all differences of relevant clinical distances result in sub-millimeter accuracy.

*indicates equal contributions
Corresponding author: Eric J. Seibel(eseibel@uw.edu)

1 Introduction

1.1 Endoscopic 3D Reconstruction

Monocular endoscopic 3D reconstruction is a challenging and widely applicable research area. High-accuracy monocular 3D reconstruction for endoscopic applications can greatly enhance the efficiency and safety of medical procedures. Approximately 500,000 Endoscopic Sinus Surgery (ESS), procedures are performed annually in the United States [1]. ESS is commonly performed on patients with chronic rhinosinusitis (CRS) refractory to medical therapy.[2, 3] This surgery involves operating near several critical anatomical structures, including cranial nerves, the dura mater, the orbit, and the internal carotid artery, presenting a risk of injury to these important areas. The overall risk of complications is estimated to be between 1% and 3% [4]. Additionally, incomplete surgical intervention can result in persistent inflammatory disease, leading to ongoing nasal symptoms in CRS patients. Incomplete surgery necessitates revision ESS which occurs in 15% to 30% of cases.[5, 6]

Image-guided surgery (IGS) systems were developed as an adjunct to ESS to assist surgeons in localizing the tip of their instrument in three axes in relation to the patient's pre-operative computed tomography (CT) scan. However, IGS relies on preoperative imaging and becomes outdated as soon as surgery begins and tissue is removed. To provide an accurate representation of changes inside the nasal cavity during surgery, intraoperative CT can be used. A prospective study of 20 CRS patients treated at an internationally renowned academic sinus center involved ESS using IGS and, prior to ending the procedure, the acquisition of additional CT imaging using an intraoperative CT scanner [7]. The intraoperative CT revealed residual bony partitions in 30% of cases, mostly in the frontal or ethmoid sinuses, which altered the surgical plan, and leading to prompt immediate intervention. However, due to the prolonged time required for intraoperative CT imaging, which can take greater than an hour use during surgery significantly increases anesthesia time, health system costs, and subjects the patient to additional radiation, significantly limiting its adoption.

In recent years, endoscopic 3D reconstruction technology has been explored as a promising alternative to intraoperative CT, offering the dual benefits of reducing radiation exposure for both patients and medical personnel while providing accurate intraoperative 3D anatomical information. Historically, researchers have employed feature-point-based 3D reconstruction methods to generate accurate 3D models from endoscopic images [8, 9, 10, 11, 12]. However, these approaches are limited by slow reconstruction speeds and difficulties in handling regions with sparse visual features. With advancements in deep learning, neural network-based methods have increasingly supplanted traditional feature-based techniques[13, 14, 15]. In ESS, Liu and colleagues introduced a monocular depth estimation method leveraging neural networks for nasal cavity 3D reconstruction, demonstrating improved performance in low-feature regions [16, 17]. Despite these advancements, recent evaluations have revealed that this approach is hindered by significant registration errors, impacting overall accuracy [18]. Furthermore, the self-supervised nature of this algorithm, which depends on initial sparse 3D reconstruction results, imposes stringent requirements on the accuracy of the initial data, thereby limiting its broader applicability.

1.2 NeRF-based 3d Reconstruction

The introduction of Neural Radiance Fields (NeRF)[19] revolutionized endoscopic 3D reconstruction technology[20, 21] generating novel views of complex scenes by learning a continuous volumetric representation from a sparse set of images. NeRF encodes a scene through a fully-connected neural network, which takes a 5D input consisting of spatial coordinates (p_x, p_y, p_z) and viewing direction (θ, ϕ) . The network outputs the corresponding volume density and emitted radiance. By sampling points along camera rays and employing volume rendering techniques, NeRF reconstructs 2D images from this volumetric data. One of the key advantages of NeRF is that it only requires input images with known camera poses for optimization, leveraging the differentiability of the volume rendering process. This approach has demonstrated superior performance in synthesizing highly realistic views of scenes with intricate geometries and complex visual properties, in comparison to previous methods in neural rendering and view synthesis.

Many extensions of NeRF have been developed to improve training speed and output quality. Instant-NGP[22], for example, accelerates training through multi-resolution hash encoding, drastically reducing optimization time. MVS-NeRF[23] enhances reconstruction quality by integrating multi-view stereo techniques, making it more effective with sparse input views. NeRF-SLAM[24] combines

NeRF with simultaneous localization and mapping (SLAM), enabling real-time scene reconstruction and camera localization. Additionally, endo-NeRF[25][26]focuses on optimizing NeRF for endoscopic imaging, further advancing the applicability of NeRF in medical scenarios. These innovations address challenges in both training efficiency and reconstruction quality, pushing NeRF-based methods towards broader real-world applications.

NeRFstudio[27] is a modular PyTorch framework designed to streamline NeRF-based research and applications. It provides plug-and-play components for implementing NeRF methods, enabling easier integration into projects. The framework supports real-time visualization, data import pipelines, and exports to video, point cloud, and mesh formats. NeRFstudio also introduced NeRFacto, a model developed as the default for real-world data captures of static scenes. Rather than being based on a single published work, NeRFacto combines elements from various methods that have proven effective with real data, offering a balanced trade-off between speed and quality. This design accelerates NeRF research and practical use in fields like computer vision, graphics, and robotics.

In this work, we developed a novel NeRF-based 3D reconstruction method that achieves high-precision 3D reconstruction in just 5-10 minutes of end-to-end processing. Our contributions are as follows:

1. **Advanced NeRF Training Framework:** We implemented an optimized NeRF training framework that accelerates the reconstruction process while maintaining high accuracy.
2. **Mono to Stereo based depth estimation:** Inspired by the NeRF-based stereo vision training network [28], we synthesized stereo vision within the NeRF-reconstructed scene from monocular endoscopic inputs and leveraged this stereo information to perform binocular depth estimation.
3. **Iterative Refinement for High-Fidelity Depth Maps:** Through multiple iterations of depth map refinement, we achieved high-fidelity depth maps, resulting in high-quality 3D reconstructions. Our results, when compared with CT data, demonstrate sub-millimeter accuracy, underscoring the effectiveness of our approach.

2 Method

In our proposed method shown in Figure1, we utilize a set of images $I = \{I_1, I_2, I_3, \dots\}$ and corresponding camera poses $P = \{p_1, p_2, p_3, \dots\}$ as the initial input to generate a raw Neural Radiance Field (NeRF) result. Simultaneously, we perform Principal Component analysis (PCA) to determine the principal direction of the camera movements. Upon the convergence of the initial NeRF, we create shifted camera poses within the reconstructed scene, with the shift direction guided by the PCA results to avoid regions with significant aliasing.

Next, we render the NeRF using both the original training poses and the shifted poses to produce stereo image pairs. These pairs are then processed using Selective-IGEV[29] to compute the disparity and subsequently, the depth maps. The depth maps obtained from the initial iteration are referred to as $Z_{\text{init}} = \{z_{\text{init}_1}, z_{\text{init}_2}, z_{\text{init}_3}, \dots, z_{\text{init}_n}\}$.

We then input Z_{init} , I , and P into a depth-supervised NeRF, using Z_{init} as the depth supervision to refine the NeRF. The same novel shifted camera poses are created as in the initial iteration, and the NeRF is rendered on both the training poses and shifted poses. Using Selective-IGEV, we obtain binocular depth maps from the first iteration, denoted as $Z_{\text{first}} = \{z_{\text{first}_1}, z_{\text{first}_2}, z_{\text{first}_3}, \dots, z_{\text{first}_n}\}$.

This iterative process continues, with depth maps from each subsequent iteration being used to further refine the NeRF. The depth maps from the second iteration are denoted as $Z_{\text{second}} = \{z_{\text{second}_1}, z_{\text{second}_2}, z_{\text{second}_3}, \dots, z_{\text{second}_n}\}$, and so on, until the depth maps converge, resulting in a final set of depth maps Z_{final} .

Finally, we conduct RGBD-fusion to achieve 3D reconstruction, combining the RGB images from $I = \{I_1, I_2, I_3, \dots\}$ with the depth maps from Z_{final} .

2.1 3D reconstruct from NeRF

Our NeRF 3D reconstruction pipeline is shown in Figure2. The camera poses of the NeRF input are five-dimensional matrices, where camera position information is demoted as $\mathbf{p} = (p_x, p_y, p_z)$ and

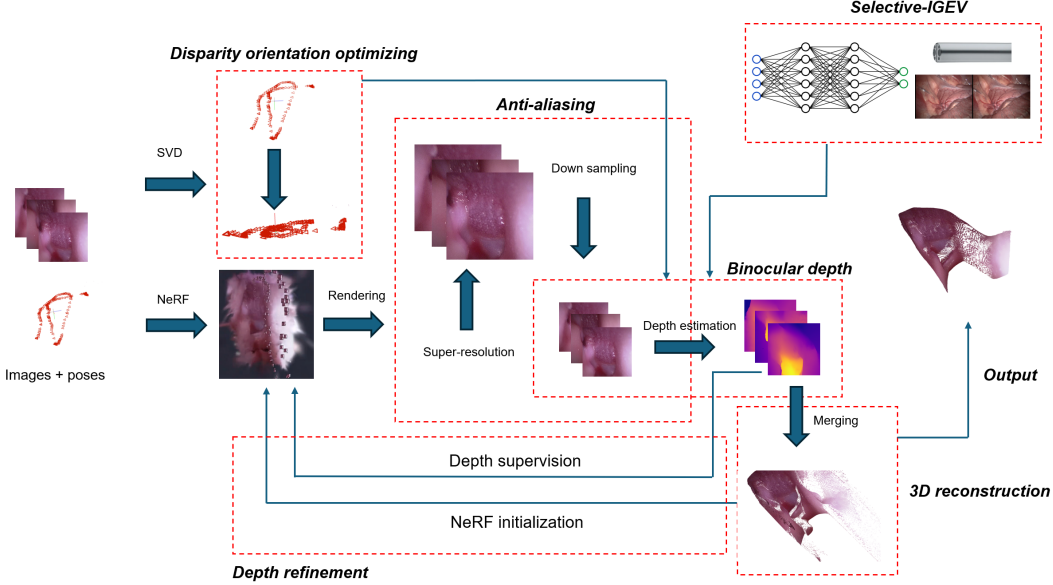


Figure 1: Overview of the proposed 3D reconstruction pipeline. This figure illustrates the full pipeline, starting from generating a raw NeRF result using image sets and camera poses derived from a monocular endoscope, then using the PCA to find the best disparity orientation and to the iterative refinement process leading to a high-accuracy depth map.

direction information is denoted as (θ, ϕ) . The camera position information (p_x, p_y, p_z) undergoes Hash Encoding for subsequent processing.[22]

$$h(x) = \bigoplus_{i=1}^d x_i \pi_i \mod N \quad (1)$$

Where \bigoplus denotes the bit-wise XOR operation, π_i represents unique large prime numbers, and N denotes the size of the hash table.

Then the encoded position information was inputted into a Multi-layer Perceptron (MLP), the output was density σ and intermediate feature ζ . The ζ at position \mathbf{p} is:

$$\zeta(\mathbf{p}) \in \mathbb{R}^{|\mathbf{k}|} \quad \text{where } \mathbf{k} = (k_\ell^m)_{\ell:0 \leq \ell \leq \ell_{\max}}^{m:-\ell \leq m \leq \ell} \quad (2)$$

Note that the total number of coefficients in \mathbf{k} is $(\ell_{\max} + 1)^2$.

The camera direction information (θ, ϕ) undergoes Spherical Harmonics Encoding[30]. Where \mathbf{k} is vector of spherical harmonics coefficients. Each element of $\zeta(\mathbf{p})$ corresponds to a coefficient $\zeta_\ell^m \in \mathbb{R}$ for the RGB components, where $0 \leq \ell < \ell_{\max}$ and $-\ell \leq m \leq \ell$. The $\mathbf{d} \in \mathbb{S}^2$ is the viewing direction and ℓ_{\max} is the maximum level of spherical harmonics. The view-dependent feature γ at a point \mathbf{p} can be determined by:

$$\gamma(\mathbf{d}) = [Y_0^0(\mathbf{d}), Y_1^{-1}(\mathbf{d}), Y_1^0(\mathbf{d}), Y_1^1(\mathbf{d}), \dots, Y_{\ell_{\max}}^{-m}(\mathbf{d}), \dots, Y_{\ell_{\max}}^m(\mathbf{d})] \quad (3)$$

where:

- $Y_\ell^m : \mathbb{S}^2 \rightarrow \mathbb{R}$ is the spherical harmonic basis function of degree ℓ and order m

After completing the Spherical Harmonics Encoding, the encoded positional information is concatenated with ζ and the appearance embedding term $\ell_i^{(a)}$ [31]. This concatenated data is then fed

into MLP_2 . Finally, through volume rendering, the ultimate RGB output is obtained. The volume rendering process is:

$$T = \sum_i \mathcal{T}_i (1 - \exp(-\sigma_i \delta_i)) c_i, \text{ where } \mathcal{T}_i = \exp\left(-\sum_{j < i} \sigma_j \delta_j\right) \quad (4)$$

$$c_i(t) = \text{MLP}_2\left(\zeta(t), \gamma(\mathbf{d}), \ell_i^{(a)}\right) \quad (5)$$

Where σ_i is the density at sample i , $\delta_i = t_i - t_{i-1}$ is the distance between consecutive samples, and c_i is the color of the sample through the pixel's ray

Using a loss function similar to that used in the original NeRF framework, we can compute Gradient. Subsequently, back-propagation updates the parameters of the MLP.

$$\mathcal{L}_{Image} = \|I - I^*\|_2^2 \quad (6)$$

Where I is the original RGB images and I^* is the rendered color image. This process concludes with the final construction of the model.

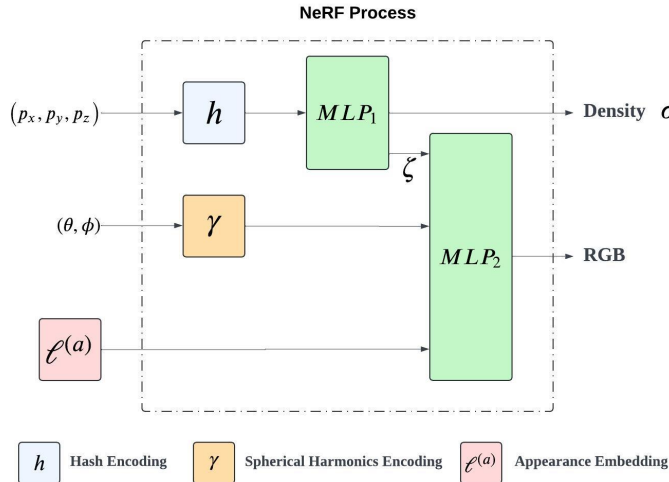


Figure 2: Novel NeRF training process. The input consists of camera position information (p_x, p_y, p_z) and direction information (θ, ϕ) . The position information is processed through MLP_1 to obtain a density σ and an intermediate feature representation ζ . This ζ , along with direction information encoded via Spherical Harmonics Encoding, is then fed into MLP_2 . Additionally, an appearance embedding term $\ell_i^{(a)}$ is incorporated to extract appearance features for more accurate visual rendering.

2.2 Mono to stereo

First, we calculate the displacement vectors from the camera poses. Given a set of camera poses $\{\mathbf{p}_1, \mathbf{p}_2, \dots, \mathbf{p}_n\}$, the displacement vectors are computed as:

$$\varphi_i = \mathbf{p}_{i+1} - \mathbf{p}_i \quad \text{for } i = 1, 2, \dots, n-1 \quad (7)$$

Let $\Phi = \{\varphi_1, \varphi_2, \dots, \varphi_{n-1}\}$ be the matrix of displacement vectors, where each row represents a displacement vector.

We perform PCA on the matrix Φ to find the principal direction of the displacements. The PCA is done by performing SVD:

$$\Phi = \mathbf{U}\Sigma\mathbf{V}^T \quad (8)$$

where: \mathbf{U} is an $(n-1) \times (n-1)$ orthogonal matrix, Σ is an $(n-1) \times 3$ diagonal matrix with singular values $\sigma_1, \sigma_2, \sigma_3$ such that $\sigma_1 \geq \sigma_2 \geq \sigma_3$, \mathbf{V} is a 3×3 orthogonal matrix whose columns are the principal components.

The first principal component \mathbf{v}_1 corresponds to the largest singular value σ_1 , and it represents the principal direction of the displacements.

Next, we project \mathbf{v}_1 onto the xy -plane to determine the primary axis of movement. The projection of \mathbf{v}_1 onto the xy -plane is given by:

$$\mathbf{v}_1^{xy} = (v_{1x}, v_{1y}, 0) \quad (9)$$

We then analyze the components v_{1x} and v_{1y} . If $|v_{1x}| > |v_{1y}|$, the primary direction is along the x -axis, and we set the translation vector \mathbf{b} as:

$$\mathbf{b} = (b, 0, 0)^T \quad (10)$$

Otherwise, if $|v_{1y}| > |v_{1x}|$, the primary direction is along the y -axis, and we set the translation vector \mathbf{b} as:

$$\mathbf{b} = (0, b, 0)^T \quad (11)$$

This process ensures that the translation vector aligns with the principal direction of camera movement, projected onto the xy -plane.

Then, we generate a virtual set of stereo extrinsic parameters $S = [E \ \mathbf{b}]$. Here, the rotation is represented by the 3×3 identity matrix E , and the translation vector $\mathbf{b} = (b, 0, 0)^T$ or $\mathbf{b} = (0, b, 0)^T$ has a magnitude b along the x or y axis in the camera reference system, depending on the results of the PCA. This configuration defines the baseline of a virtual stereo camera.

Next, we generate two novel views: one from a training viewpoint $M_i = [R_i | t_i]$ and the other from its corresponding virtual stereo camera viewpoint $M_i^R = M_i \times S = [R_i | (t_i + b)]$. These views serve as the reference and target frames of a perfectly rectified stereo pair, with the target frame positioned to the right of the reference frame. This method enables the creation of numerous stereo samples for stereo depth estimation.

2.3 Stereo Depth Estimation

In this subsection, we focus on stereo depth estimation using Selective-IGEV. Initially, we render the NeRF from both the original training poses and the newly created shifted poses to produce stereo image pairs. These pairs are then input into the Selective-IGEV[29] model to predict the disparity map.

The disparity d between the stereo pairs is calculated using the Selective-IGEV model. The depth z can be derived using the formula:

$$z = \frac{f \cdot B}{d} \quad \text{with} \quad 3B < z < 10B \quad (12)$$

where: z is the depth, f is the focal length of the camera, B is the baseline distance between the stereo camera pair, d is the disparity value from the disparity map.

Because stereo cameras have significant errors at very close and very far distances, we select only the depths in the range $3 \cdot B < z < 10 \cdot B$.

2.4 Depth Iteration

The depth iteration process in NeRF[32] involves refining depth supervision through multiple cycles. Initially, images with their associated camera matrices $P = \{\mathbf{p}_1, \mathbf{p}_2, \mathbf{p}_3, \dots\}$ are used to generate an initial NeRF model. From this model, depth maps are derived using stereo depth estimation, which we denote as $Z_{\text{init}} = \{z_{\text{init}_1}, z_{\text{init}_2}, z_{\text{init}_3}, \dots, z_{\text{init}_n}\}$ from the first iteration.

For each image I_j and its corresponding camera matrix \mathbf{p}_j , the depth of the visible points in z_{init_j} is estimated by projecting these points onto the image plane using \mathbf{p}_j . The resulting depth z'_{ij} corresponds to the re-projected z value. However, these depth estimates z'_{ij} may be noisy due to factors such as inaccurate correspondences or inaccurate disparity estimation from Selective-IGEV.

To address this noise, the depth value z'_{ij} is modeled as a random variable with a Gaussian distribution centered around the estimated depth, with variance $\hat{\sigma}_i$: $z'_{ij} \sim \mathcal{N}(z'_{ij}, \hat{\sigma}_i)$. The goal is to minimize the Kullback-Leibler (KL) divergence between the ideal ray termination distribution and the noisy depth distribution at the image coordinates corresponding to Z_{init_j} .

This process leads to the depth supervision loss $\mathcal{L}_{\text{Depth}}$, which integrates the probabilistic depth information derived from the stereo estimation. The loss is calculated as:

$$\begin{aligned} \mathcal{L}_{\text{Depth}} &= \mathbb{E}_{z_i \in Z_j} \left[\int \log h(t) \exp \left(-\frac{(t - z'_{ij})^2}{2\hat{\sigma}_i^2} \right) dt \right] \\ &\approx \mathbb{E}_{z_i \in Z_j} \left[\sum_k \log h_k \exp \left(-\frac{(t_k - z'_{ij})^2}{2\hat{\sigma}_i^2} \right) \Delta t_k \right]. \end{aligned} \quad (13)$$

The overall loss function for training NeRF is then defined as:

$$\mathcal{L} = \mathcal{L}_{\text{Image}} + \lambda_z \mathcal{L}_{\text{Depth}}, \quad (14)$$

where λ_z is a hyper-parameter that balances the contributions of color and depth supervision losses.

The application of this depth supervision loss $\mathcal{L}_{\text{Depth}}$ leads to an optimized NeRF model. Once this optimized NeRF model is obtained, the process described in steps 2.2 to 2.4 is repeated on this newly optimized model. Specifically, a new set of depth maps Z_{first} is derived from this optimized NeRF model using the same stereo depth estimation process. The depth map Z_{first} is then used as the supervised depth input for the next iteration of NeRF refinement.

In each subsequent iteration, the process is repeated: the optimized NeRF model is further refined using the updated depth map from the previous iteration, leading to a new depth map (e.g., Z_{second} , Z_{third} , etc.). This iterative process continues, with each cycle producing a progressively refined NeRF model and corresponding depth map, until the changes in the depth map become negligible, indicating convergence. The final depth map Z_{final} and the corresponding NeRF model represent the optimized result after the iterative refinement process.

3 Experiments

In this experiment, we collected video data using the HOPKINS Telescope 0° nasal endoscope (Karl Storz, Tuttlingen, Germany) and exported high-definition video via the Karl Storz IMAGE1 S 4U 4k camera system. The resolution and frame rate of the exported data were 1080p at 27 Hz. The nasal phantom used was a high-fidelity model produced by FuseTec (Adelaide, Australia), and the 3D reconstruction ground truth for this experiment was based on a CT model, scanned at a resolution of 0.625 mm slice thickness.

Camera poses were obtained using two methods: COLMAP and an NDI electromagnetic tracker. The EM tracker used in this study was the NDI 3D Guidance Model 90 Sensor, an electromagnetic sensor capable of providing 6DOF tracking.

The workstation for training NeRF was equipped with an AMD Ryzen 7950x CPU and an RTX 4080 Super GPU. The NeRF model was trained for 10,000 epochs per iteration.

The total end-to-end pipeline training time was dependent on the length of the video. Typically, we used video clips ranging from 5 to 10 seconds in duration, with the overall 3D reconstruction process taking approximately 5 to 10 minutes.

4 Results

In this section, we manually registered the 3D reconstruction results with the CT model and employed the measurement tools integrated within 3D Slicer to assess their accuracy. The superimposition of the 3D reconstruction and CT model is depicted in Figure 3 B. The green mesh represents the endoscopic 3D reconstruction, while the white mesh corresponds to the CT model. The alignment between the white and green meshes demonstrates a high degree of structural fidelity in our 3D reconstruction. To quantitatively evaluate the accuracy of our reconstruction, we manually measured the spatial distances between the endoscopic 3D reconstruction and corresponding points in the CT data. In the 2D view, we specifically selected regions exhibiting the largest deviations as well as those with average deviations, as illustrated in Figure 3 A, C, and D.

Upon conducting distance measurements within the sectional view, we determined that the majority of points attained reconstruction errors less than 1mm, with the maximum recorded error less than 2 mm. These findings verify that the accuracy of our algorithm substantially surpasses that of the current SOTA methodologies[18].

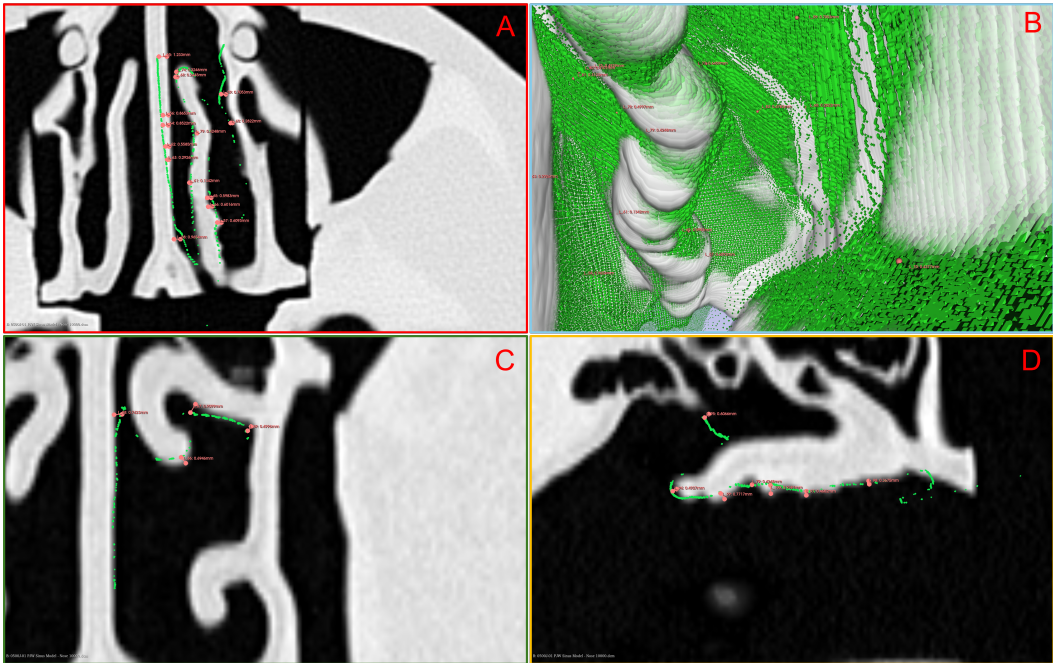


Figure 3: Comparison between 3D reconstruction and CT model. Figure 3B displays the 3D reconstruction’s green mesh aligned with the CT model’s white mesh. Additional figures A, C, and D show the 3D reconstruction and CT model alignment from different fixed viewpoints.

In addition to comparing point-to-point accuracy with CT data, key anatomical structures that serve critical importance to ESS are also measured. Bony landmarks are static during surgery and offer reliable reference points. Accurate measurements of these pivotal structures are crucial, as they directly impact the surgeon’s ability to navigate complex procedures and ensure optimal outcomes.

In the present study, we meticulously quantified the distance represented by a coronal plane perpendicular to the posterior aspect of the nasolacrimal duct and extending medially to the intersection with the nasal septum. Figure 4 elucidates the frontal and axial views employed during the measurement procedure.

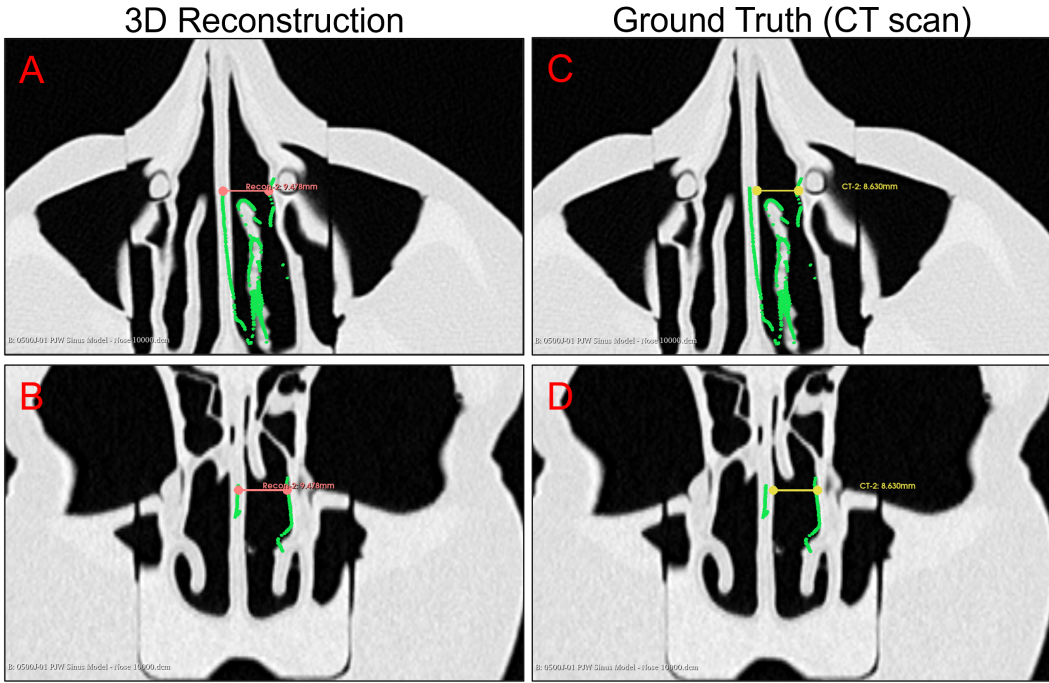


Figure 4: Measurement of key anatomical structures in the nasal cavity. Subfigures A and B depict the measurements taken from the 3D reconstruction, while subfigures C and D illustrate the corresponding measurements from the CT results. These measurements are critical for surgical planning, with results compared across five slices as depicted in Table 1.

Table 1: measurements

Measurements	Length(mm)	Discrepancy(mm)
3d Recon - 1 CT- 1	9.478 8.630	+0.848
3d Recon - 2 CT- 2	9.468 8.553	+0.915
3d Recon - 3 CT- 3	9.483 8.605	+0.878
3d Recon - 4 CT- 4	9.582 8.819	+0.763
3d Recon - 5 CT - 5	9.785 8.835	+0.950
<hr/>		
Average	Length(mm)	Discrepancy(mm)
3D Recon CT	9.5592 8.6884	+0.8708

We conducted measurements across five different slices to assess the distance between the posterior aspect of the nasolacrimal duct and the nasal septum, as illustrated in Table 1. The mean length obtained through CT measurements was 8.6884 mm, while the mean length derived from 3D reconstruction was 9.5592 mm, yielding an average discrepancy of merely 0.8708 mm. This result unequivocally demonstrates that our method achieves sub-millimeter accuracy even in the evaluation of anatomically critical regions, underscoring its potential for high-accuracy measurements in clinically significant contexts.

5 Ablation study

In this section, our ablation study focuses on two key analyses: the impact of multiple NeRF iterations and the effectiveness of using PCA to identify the direction of disparity generation. Figure 5 illustrates the influence of iterative NeRF processing. We observed that with an increasing number of NeRF iterations, the depth maps exhibit enhanced layering and improved resolution. From the initial iteration (iteration 0, no refinement) to iteration 2, the most pronounced enhancement in depth map resolution was observed between iteration 0 and iteration 1. During this phase, several regions with previously indistinct differentiation transitioned into areas with clearly defined boundaries. Concurrently, the areas corresponding to depths less than three times the baseline and those exceeding ten times the baseline exhibited measurable changes, signifying that the iterative process substantially influenced the depth map’s structure. In contrast, from iteration 1 to iteration 2, the areas within these depth ranges remained relatively stable; however, the overall resolution of the depth maps continued to improve, with structural delineations becoming increasingly prominent. This figure qualitatively illustrates the iterative refinement of depth maps, underscoring that the NeRF-based iterative strategy is effective in optimizing both the resolution and accuracy of depth estimations.

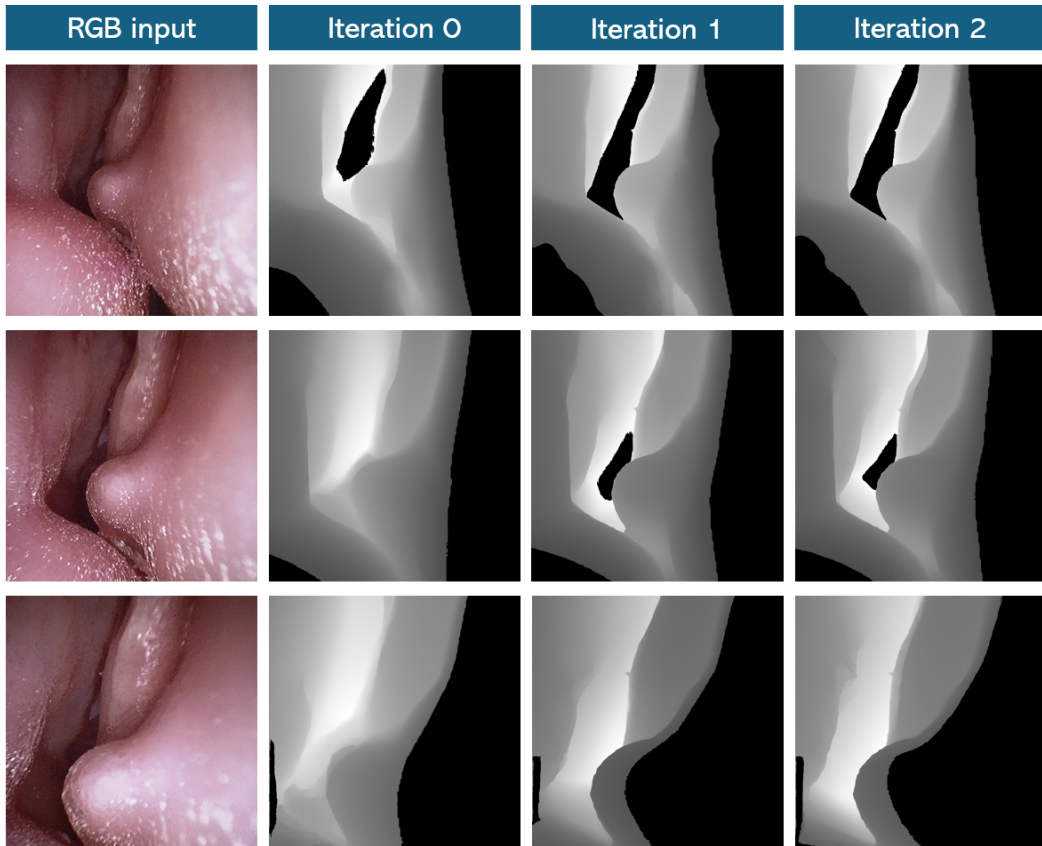


Figure 5: Impact of iterative NeRF refinement on depth map resolution. This figure qualitatively shows how depth maps evolve from the 0th iteration (no refinement) to the 2nd iteration, demonstrating substantial improvements in depth resolution and layering, particularly between the 0th and 1st iterations.

When analyzing the utility of employing a PCA-based strategy to determine the optimal direction for disparity generation, we utilized binocular disparity maps instead of depth maps, as they offer a more intuitive representation of the impact of the PCA strategy. The results are illustrated in 6, where the left image demonstrates the outcome of applying the PCA strategy. In this scenario, the binocular disparity was generated by translating the camera along the principal direction of motion, resulting in a disparity map that is both clean and well-structured. In contrast, the right image presents the results without the use of the PCA strategy, where the disparity map was created by directly translating the

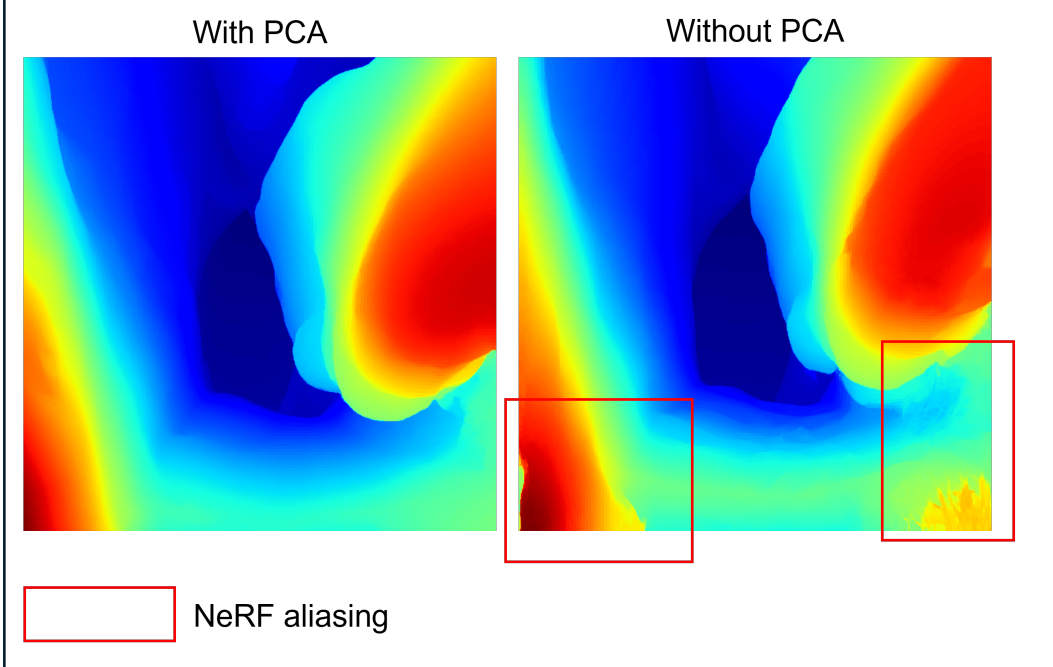


Figure 6: Disparity map comparison using PCA-based and non-PCA-based strategies. The left image demonstrates the clean disparity map generated by translating the camera along the principal motion direction determined by PCA, while the right image shows aliasing artifacts caused by generating disparity along an unsupported direction without PCA.

camera pose to the right. Notably, in the regions highlighted by the red box, a significant amount of NeRF aliasing is present, which undermines the accuracy of the depth map. This aliasing occurs because there are insufficient training views along the direction in which the disparity is generated. NeRF models generally perform reliably only in regions where the viewpoints are sufficiently covered during training; otherwise, overfitting occurs, leading to high-fidelity renderings only near the trained viewpoints. When the camera is moved along a direction with insufficient viewpoint coverage and a disparity map is rendered, the result manifests conspicuous aliasing artifacts. However, by applying the PCA strategy, the direction in which the disparity is generated aligns with the principal motion direction, where multiple training views are available. This resolves the issue of insufficient viewpoint coverage along the disparity generation axis, thereby producing a disparity map devoid of aliasing artifacts.

6 Conclusion

This research introduces a novel, high-accuracy 3D reconstruction pipeline tailored for conventional monocular endoscopic applications. By incorporating NeRF with hash encoding, spherical harmonics encoding and appearance embedding, we have successfully achieved both rapid and high-fidelity reconstructions. Subsequently, we utilized PCA to determine the principal direction of camera movement and generated disparity by translating along this direction. The depth map obtained through binocular depth estimation was then employed as depth supervision to retrain and refine the NeRF model, further improving its output. This iterative process, where depth maps are progressively optimized, enabled us to achieve sub-millimeter accuracy in 3D reconstructions of the nasal cavity, meeting clinical standards for surgical applications. Moreover, the entire end-to-end process requires only 5 to 10 minutes, which provides a potentially more convenient and robust alternative to intraoperative CT scans, highlighting the strong potential for real-world medical applications.

However, a current limitation of this pipeline is that it remains a non-real-time solution. In future work, we aim to address this by integrating the proposed pipeline with SLAM (Simultaneous Localization and Mapping) or visual odometry techniques, with the goal of enabling real-time, high-accuracy

3D reconstruction. This advancement would further broaden the clinical applicability of the system, allowing for seamless integration into time-sensitive surgical environments. Additionally, we plan to extend this methodology to explore its applications in the bronchial and intestinal contexts. By applying our approach to these areas, we hope to enhance its utility across a wider range of minimally invasive procedures, thereby contributing to the ongoing evolution of medical technology. Through these efforts, we aspire to provide more efficient 3D reconstruction solutions for complex internal structures, ultimately improving clinical outcomes and patient safety.

References

- [1] Neil Bhattacharyya. Ambulatory sinus and nasal surgery in the united states: demographics and perioperative outcomes. *The Laryngoscope*, 120(3):635–638, 2010.
- [2] Lee C Young, Nicholas W Stow, Lifeng Zhou, and Richard G Douglas. Efficacy of medical therapy in treatment of chronic rhinosinusitis. *Allergy & Rhinology*, 3(1):ar–2012, 2012.
- [3] Richard R Orlandi, Todd T Kingdom, Peter H Hwang, Timothy L Smith, Jeremiah A Alt, Fuad M Baroody, Pete S Batra, Manuel Bernal-Sprekelsen, Neil Bhattacharyya, Rakesh K Chandra, et al. International consensus statement on allergy and rhinology: rhinosinusitis. In *International forum of allergy & rhinology*, volume 6, pages S22–S209. Wiley Online Library, 2016.
- [4] James A Stankiewicz, Devyani Lal, Matthew Connor, and Kevin Welch. Complications in endoscopic sinus surgery for chronic rhinosinusitis: a 25-year experience. *The Laryngoscope*, 121(12):2684–2701, 2011.
- [5] Muaid I Aziz Baban, Baidaa Mirza, and Paolo Castelnuovo. Radiological and endoscopic findings in patients undergoing revision endoscopic sinus surgery. *Surgical and Radiologic Anatomy*, 42:1003–1012, 2020.
- [6] Kristine A Smith, Richard R Orlandi, Gretchen Oakley, Huong Meeks, Karen Curtin, and Jeremiah A Alt. Long-term revision rates for endoscopic sinus surgery. In *International forum of allergy & rhinology*, volume 9, pages 402–408. Wiley Online Library, 2019.
- [7] Alexis H Jackman, James N Palmer, Alexander G Chiu, and David W Kennedy. Use of intraoperative ct scanning in endoscopic sinus surgery: a preliminary report. *American journal of rhinology*, 22(2):170–174, 2008.
- [8] Nader Mahmoud, Iñigo Cirauqui, Alexandre Hostettler, Christophe Doignon, Luc Soler, Jacques Marescaux, and Jose Maria Martinez Montiel. Orbslam-based endoscope tracking and 3d reconstruction. In *Computer-Assisted and Robotic Endoscopy: Third International Workshop, CARE 2016, Held in Conjunction with MICCAI 2016, Athens, Greece, October 17, 2016, Revised Selected Papers 3*, pages 72–83. Springer, 2017.
- [9] Chen Gong, Yaxuan Zhou, Andrew Lewis, Pengcheng Chen, Jason R Speich, Michael P Porter, Blake Hannaford, and Eric J Seibel. Real-time camera localization during robot-assisted telecystoscopy for bladder cancer surveillance. *Journal of Medical Robotics Research*, 7(02n03):2241002, 2022.
- [10] Pengcheng Chen, Chen Gong, Andrew Lewis, Yaxuan Zhou, Seyed Mohammad Mohaghegh Poor, Blake Hannaford, and Eric J Seibel. Real-time flexible endoscope navigation within bladder phantom having sparse non-distinct features is enhanced with robotic control. In *Medical Imaging 2022: Image-Guided Procedures, Robotic Interventions, and Modeling*, volume 12034, pages 68–83. SPIE, 2022.
- [11] Kristen L Lurie, Roland Angst, Dimitar V Zlatev, Joseph C Liao, and Audrey K Ellerbee Bowden. 3d reconstruction of cystoscopy videos for comprehensive bladder records. *Biomedical optics express*, 8(4):2106–2123, 2017.
- [12] Andrew Lewis, Chen Gong, Yaxuan Zhou, Pengcheng Chen, Michael P Porter, Blake Hannaford, and Eric J Seibel. Real time localization of cystoscope angulation in 2d bladder phantom for telecystoscopy. In *2021 International Symposium on Medical Robotics (ISMR)*, pages 1–8. IEEE, 2021.
- [13] Kutsev Bengisu Ozyoruk, Guliz Irem Gokceler, Taylor L Bobrow, Gulfize Coskun, Kagan Inctan, Yasin Almalioğlu, Faisal Mahmood, Eva Curto, Luis Perdigoto, Marina Oliveira,

et al. Endoslam dataset and an unsupervised monocular visual odometry and depth estimation approach for endoscopic videos. *Medical image analysis*, 71:102058, 2021.

[14] Beilei Cui, Mobarakol Islam, Long Bai, and Hongliang Ren. Surgical-dino: adapter learning of foundation models for depth estimation in endoscopic surgery. *International Journal of Computer Assisted Radiology and Surgery*, pages 1–8, 2024.

[15] David Recasens, José Lamarca, José M Fácil, JMM Montiel, and Javier Civera. Endo-depth-and-motion: Reconstruction and tracking in endoscopic videos using depth networks and photometric constraints. *IEEE Robotics and Automation Letters*, 6(4):7225–7232, 2021.

[16] Xingtong Liu, Maia Stiber, Jindan Huang, Masaru Ishii, Gregory D Hager, Russell H Taylor, and Mathias Unberath. Reconstructing sinus anatomy from endoscopic video—towards a radiation-free approach for quantitative longitudinal assessment. In *Medical Image Computing and Computer Assisted Intervention—MICCAI 2020: 23rd International Conference, Lima, Peru, October 4–8, 2020, Proceedings, Part III 23*, pages 3–13. Springer, 2020.

[17] Xingtong Liu, Ayushi Sinha, Masaru Ishii, Gregory D Hager, Austin Reiter, Russell H Taylor, and Mathias Unberath. Dense depth estimation in monocular endoscopy with self-supervised learning methods. *IEEE transactions on medical imaging*, 39(5):1438–1447, 2019.

[18] Jan Emily Mangulabnan, Roger D Soberanis-Mukul, Timo Teufel, Isabela Hernández, Jonas Winter, Manish Sahu, Jose L Porras, S Swaroop Vedula, Masaru Ishii, Gregory Hager, et al. A quantitative evaluation of dense 3d reconstruction of sinus anatomy from monocular endoscopic video. *arXiv preprint arXiv:2310.14364*, 2023.

[19] Ben Mildenhall, Pratul P. Srinivasan, Matthew Tancik, Jonathan T. Barron, Ravi Ramamoorthi, and Ren Ng. Nerf: representing scenes as neural radiance fields for view synthesis. *Commun. ACM*, 65(1):99–106, December 2021.

[20] Pengcheng Chen, Nicole M Gunderson, Andrew Lewis, Jason R Speich, Michael P Porter, and Eric J Seibel. Enabling rapid and high-quality 3d scene reconstruction in cystoscopy through neural radiance fields. In *Medical Imaging 2024: Image-Guided Procedures, Robotic Interventions, and Modeling*, volume 12928, pages 350–359. SPIE, 2024.

[21] Belén Lojo Rodríguez, Guilherme Lopes Borges, Marta López-Brea García, Anne Schützenberger, and Andreas M Kist. Neural radiance fields for 3d reconstruction in monoscopic laryngeal endoscopy. In *2024 IEEE International Symposium on Biomedical Imaging (ISBI)*, pages 1–5. IEEE, 2024.

[22] Thomas Müller, Alex Evans, Christoph Schied, and Alexander Keller. Instant neural graphics primitives with a multiresolution hash encoding. *ACM transactions on graphics (TOG)*, 41(4):1–15, 2022.

[23] Anpei Chen, Zexiang Xu, Fuqiang Zhao, Xiaoshuai Zhang, Fanbo Xiang, Jingyi Yu, and Hao Su. Mvsnerf: Fast generalizable radiance field reconstruction from multi-view stereo. In *Proceedings of the IEEE/CVF International Conference on Computer Vision (ICCV)*, pages 14124–14133, October 2021.

[24] Antoni Rosinol, John J. Leonard, and Luca Carlone. Nerf-slam: Real-time dense monocular slam with neural radiance fields. In *2023 IEEE/RSJ International Conference on Intelligent Robots and Systems (IROS)*, pages 3437–3444, 2023.

[25] Yuehao Wang, Yonghao Long, Siu Hin Fan, and Qi Dou. Neural rendering for stereo 3d reconstruction of deformable tissues in robotic surgery. In *International conference on medical image computing and computer-assisted intervention*, pages 431–441. Springer, 2022.

[26] Yuehao Wang, Bingchen Gong, Yonghao Long, Siu Hin Fan, and Qi Dou. Efficient endonerf reconstruction and its application for data-driven surgical simulation. *International Journal of Computer Assisted Radiology and Surgery*, 19(5):821–829, 2024.

[27] Matthew Tancik, Ethan Weber, Evonne Ng, Ruilong Li, Brent Yi, Terrance Wang, Alexander Kristoffersen, Jake Austin, Kamyar Salahi, Abhik Ahuja, David Mcallister, Justin Kerr, and Angjoo Kanazawa. Nerfstudio: A modular framework for neural radiance field development. In *ACM SIGGRAPH 2023 Conference Proceedings, SIGGRAPH '23, New York, NY, USA, 2023*. Association for Computing Machinery.

[28] Fabio Tosi, Alessio Tonioni, Daniele De Gregorio, and Matteo Poggi. Nerf-supervised deep stereo. In *Proceedings of the IEEE/CVF conference on computer vision and pattern recognition*, pages 855–866, 2023.

- [29] Xianqi Wang, Gangwei Xu, Hao Jia, and Xin Yang. Selective-stereo: Adaptive frequency information selection for stereo matching. In *Proceedings of the IEEE/CVF Conference on Computer Vision and Pattern Recognition (CVPR)*, pages 19701–19710, June 2024.
- [30] Alex Yu, Ruilong Li, Matthew Tancik, Hao Li, Ren Ng, and Angjoo Kanazawa. Plenoctrees for real-time rendering of neural radiance fields. In *Proceedings of the IEEE/CVF International Conference on Computer Vision (ICCV)*, pages 5752–5761, October 2021.
- [31] Ricardo Martin-Brualla, Noha Radwan, Mehdi S. M. Sajjadi, Jonathan T. Barron, Alexey Dosovitskiy, and Daniel Duckworth. Nerf in the wild: Neural radiance fields for unconstrained photo collections. In *Proceedings of the IEEE/CVF Conference on Computer Vision and Pattern Recognition (CVPR)*, pages 7210–7219, June 2021.
- [32] Kangle Deng, Andrew Liu, Jun-Yan Zhu, and Deva Ramanan. Depth-supervised nerf: Fewer views and faster training for free. In *Proceedings of the IEEE/CVF Conference on Computer Vision and Pattern Recognition*, pages 12882–12891, 2022.